applied sciences

MDPI

Article

Local Temperature Development in the Fracture Zone during Uniaxial Tensile Testing at High Strain Rate: Experimental and Numerical Investigations

Elmar Galiev [1,*], Sven Winter [1], Franz Reuther [1], Verena Psyk [1], Marc Tulke [2], Alexander Brosius [2] and Verena Kräusel [1]

[1] Fraunhofer Institute for Machine Tools and Forming Technology IWU, Reichenhainer Strasse 88, 09126 Chemnitz, Germany; sven.winter@iwu.fraunhofer.de (S.W.); franz.reuther@iwu.fraunhofer.de (F.R.); verena.psyk@iwu.fraunhofer.de (V.P.); verena.kraeusel@iwu.fraunhofer.de (V.K.)

[2] Chair of Forming and Machining Processes (FF), Technische Universität Dresden, 01062 Dresden, Germany; marc.tulke@tu-dresden.de (M.T.); alexander.brosius@tu-dresden.de (A.B.)

* Correspondence: elmar.galiev@iwu.fraunhofer.de

Abstract: The quality of simulation results significantly depends on the accuracy of the material model and parameters. In high strain rate forming processes such as, e.g., electromagnetic forming or adiabatic blanking, two superposing and opposing effects influence the flow stress of the material: strain rate hardening and thermal softening due to adiabatic heating. The presented work contributes to understanding these influences better by quantifying the adiabatic heating of the workpiece during deformation and failure under high-speed loading. For this purpose, uniaxial tensile tests at different high strain rates are analyzed experimentally and numerically. A special focus of the analysis of the tensile test was put on identifying a characteristic time- and position-dependent strain rate. In the experiments, in addition to the measurement of the force and elongation, the temperature in the fracture region is recorded using a thermal camera and a pyrometer for higher strain rates. Simulations are carried out in LS-Dyna using the GISSMO model as a damage and failure model. Both experimental and simulated results showed good agreement regarding the time-dependent force-displacement curve and the maximum occurring temperature.

Keywords: numerical simulation; high-speed forming; DC06; material properties

Citation: Galiev, E.; Winter, S.; Reuther, F.; Psyk, V.; Tulke, M.; Brosius, A.; Kräusel, V. Local Temperature Development in the Fracture Zone during Uniaxial Tensile Testing at High Strain Rate: Experimental and Numerical Investigations. *Appl. Sci.* **2022**, *12*, 2299. https://doi.org/10.3390/app12052299

Academic Editor: Marco Sasso

Received: 26 January 2022
Accepted: 18 February 2022
Published: 22 February 2022

1. Introduction

High-speed production processes such as electromagnetic or electrohydraulic forming and high-speed impact cutting have a high potential for industrial production because of the many advantages compared with standard processes, such as high deformation capacity, high shear quality, etc. [1–3]. It is well known that the availability of an accurate FEM modeling for molding processes is a key means for industrial implementation of technologies and therefore enables the exploitation of process-specific advantages. In general, modern process simulation requires constitutive material models to describe plasticity. These models must reflect the essential relationships between yield strength and stress state, strain, strain rate, and temperature for the specific material. In addition to the description of the yield surface as part of the plasticity characteristic, this includes the isotropic or kinematic hardening law, which is basically an empirical functional dependence on strain, strain rate, and material temperature. In order to account for the strain rate sensitivity of materials, material models that are optimized for high-speed processes and that take into account the strain-rate sensitivity of the materials can be used.

Starting from a range of relatively low strain rates between 0.01/s and 0.1/s, significant differences in material behavior can already be seen, as shown by the example of steel 316 L in [4]. In [5], the effect of sensitivity to the strain rate of various types of high-strength

steels, in the range of strain rates from quasi-static to 200/s, was considered. In this study, a dependence in the form of a 10% increase in the yield strength value of the material with a six-fold increase in the strain rate was found. A higher range of strain rates of up to 10^3/s was investigated in [6] using TWIP steel as an example, and the instantaneous strain rate sensitivity (ISRS), which changes with strain rate hopping due to thermally activated dislocation motion dominated by intergranular carbon atoms, was examined. Therefore, it is also important to evaluate the effect and the development of temperature changes in samples with different strain rates [7].

Apart from the strain rate influence on the material plasticity, it is equally important to use fracture models that take into account the strain rate for modeling high-speed deformation processes. Many currently known damage and fracture models allow for the dependence of the fracture strain on the strain rate. For example, the fracture criterion in the Johnson–Cook model [8] describes a plasticity and damage model based on the Gourson flow surface taking strain rate into account. Another common example is the Gurson damage model [9], with an extension by Tvergaard and Needleman [9,10], based on a micromechanical model describing growth and nucleation of spheroidal cavities in rigid plastic materials. In combination with the forming simulation, the calculated void volume fraction f serves as a damage parameter for crash simulation [11]. Other purely phenomenologically motivated models with directly defined fracture surface curves, such as GISSMO, offer the possibility of scaling and modifying these curves or surfaces depending on the strain rate [12,13]. Given the strain rate dependence, in some cases, a non-self-similar shift of the fracture curves or fracture surfaces may be required. This means that constant scaling of the fracture strain-rate-dependent fracture curve is not sufficient and it is reasonable to use a triaxial modification, for example.

For modeling both plasticity and damage in addition to strain rate, temperature effects are also decisive. In forming technology, a large part (85–95%) of the energy introduced into the workpiece is converted into heat. Especially at high forming speeds and correspondingly short process times, the heat generated can hardly be dissipated from the material, resulting in quasiadiabatic behavior. This means, that even without external heating of the semi-finished parts, a high-speed forming process is carried out at a higher temperature compared with a quasistatic process, which can lead to significant thermal softening of the material. This is especially relevant when it comes to localization and a correspondingly strong increase in the local strain, strain rate, and temperature. An exemplary application where this effect becomes relevant is the formation of adiabatic shear bands in high-speed impact cutting [14]. The two effects of strain hardening and thermal softening superpose each other so that accurate and thermo-mechanically consistent material modeling is complicated significantly.

As part of previous work [15], a method was developed for the determination of material and failure characteristics for processes with high forming speeds including extremely high strain rates in the range of more than 10^4/s, using DC06 steel and AW5754 aluminum alloy as examples. The calculation of the values was performed by testing samples of different stress states, using an electromagnetically accelerated hammer and following inverse simulation of the process. An interesting observation from this study is a significantly higher strain rate sensitivity of tensile specimens compared with shear specimens in the case of DC06 steel. However, as temperature has been disregarded in the inverse parameter identification, adiabatic heating is not considered, which leads to an overestimation of the stresses and a simultaneous underestimation of the strains. Additionally, it must be taken into account that due to the strong localization of the strains and the temperature increase, the meshing significantly affects the accuracy of the simulation. With increasing element size, temperature peaks can no longer be modeled correctly, which leads to a significant underestimation of the occurring temperature [16–18].

The topic of local temperature change in the deformation zone during uniaxial tension has always been extremely important and in the early stages could be obtained using analytical calculations and simplified models [19]. Later in [20], the effects of initial geo-

metrical defects and thermal gradients on the tensile stress and strain behavior in FEM simulations of uniaxial tensile tests were investigated. Thus, the temperature calculation in the deformation region is based on the measurement of the plastic work fraction and its subsequent conversion into heat (also referred to as the inelastic heat fraction (IHF)). In [21], also using the example of a uniaxial test bar, it was proved that the IHF is not constant depending on the plastic strain, and in addition, is also sensitive to changes in the strain rate. In the study [22], monotonic loading in uniaxial tension tests was investigated using a digital image correlation system in conjunction with infrared thermography. However, this study was only carried out for relatively lower strain rates.

Altogether, the development and change of temperature in the fracture region of a material is extremely important and can explain many of the effects occurring in the material, often considered as an effect of the strain rate. These two important concepts, temperature and strain rate dependence, are fundamental for the creation of a material model that is close to the real process. In the area of high strain rates, everything is much more complicated because measuring equipment is restricted with regard to measuring frequency and the area where the local temperature maximum is reached shortly before the material fracture is relatively small.

Thus, the main goal and motivation of this work are to provide a deeper understanding of the superposing and opposing influences of strain rate and temperature on the material behavior in high-speed forming by quantifying the adiabatic heating of the workpiece during deformation and failure under high-speed loading. For this purpose, uniaxial tensile tests at different high strain rates are analyzed experimentally and numerically. A special focus of the analysis of the tensile test is put on identifying a characteristic time- and position-dependent strain rate. In the experiments, in addition to the measurement of the force and elongation, the temperature in the fracture region is recorded using a thermal camera and a pyrometer for higher strain rates. Simulations are carried out in LS-Dyna. Based on the described previous work, a material model for numerically simulating high-speed forming processes, taking into account plasticity and fracture parameters, is provided. By initially evaluating the comparability of the plastic component of the obtained strain-rate-dependent model with the experimental data, it can also be used to estimate the resulting deformation temperature, even in the fracture zone where the maximum strain rate and temperature occurs. This, in turn, will enable use of a simplified method for thermomechanical calculation, namely, the conversion of strain energy into temperature, to estimate the temperature of the simulated high-speed molding processes as close to reality as possible. In conjunction with this, it is important to pre-estimate the temperature development for different strain rates, for further validation of the simulation data.

2. Materials and Methods

2.1. Material

This study uses commercial DC06 (1.0873) steel sheets which were cold rolled to 1 mm thickness. This material has a wide industrial application and features significant strain rate dependency [15]. Table 1 shows the chemical composition (in wt %). The mechanical properties, received from the material supplier of the investigated material at quasistatic load, are shown in Table 2.

Table 1. Chemical compositions of the investigated DC06 steel.

Alloy Code	Composition (wt %)							
DC06	C	Si	Mn	S	Al	Ti	Nb	Fe
	0.007	0.017	0.122	0.008	0.06	0.06	0.01	bal.

Table 2. Mechanical properties of the material sheet at quasistatic load.

Grade	$R_{p0.2}$ (MPa)	R_m (MPa)	A_{80} (%)
DC06	137	291	41

2.2. Experimental Setup

For our investigation, a simple experimental setup that allows comprehensive observation of a high-speed deformation was necessary. Therefore, it was focused on high-speed tensile tests carried out in a commercial high-speed testing machine, Zwick HTM 16020. The geometric shape of the specimen is shown in Figure 1. This geometry is optimized for use on the high-speed test machine from Zwick and proved to be suitable in previous experiments. The asymmetrical specimen shape results from the test principle of the Zwick/Roell 16020 high-speed materials testing machine used. To achieve the very high test speeds of up to 20 m/s or strain rates of 1000/s, an acceleration distance is required, which is realized over the upper specimen length.

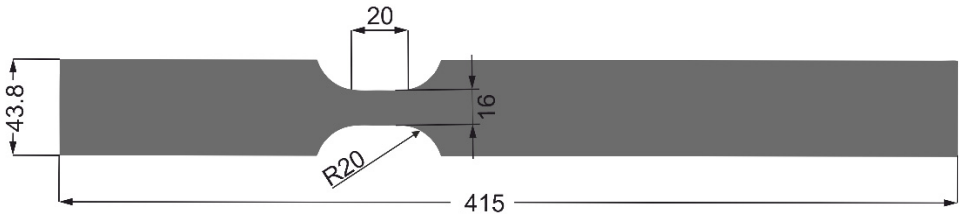

Figure 1. Schematic drawing of a sample in mm.

Furthermore, there is an end-position damping that must be added to this distance. The thickness of the samples is 1 mm, the measurement length is 20 mm, and the width in the thinning area is 16 mm. Three samples were tested for each of the strain rates considered.

In the uniaxial tensile test, the nominal strain rate can be calculated directly from the nominal traverse velocity, v, with knowledge of the measurement length, L, via Equation (1).

$$d\varepsilon/dt = v/L \quad (1)$$

The tests are performed at constant nominal test speeds v = 0.002 m/s (nominal strain rate 0.1/s), v = 0.1 m/s (nominal strain rate 5/s), v = 1 m/s (nominal strain rate 50/s), v = 4 m/s (nominal strain rate 200/s), and v = 20 m/s (nominal strain rate 1000/s). The strain in the measuring area is optically recorded by an extensometer Rudolf 200XR. Therefore, the front side of the specimen is primed white and the measuring area is painted black, creating sharply defined lines that can be easily detected by the extensometer, as shown in Figure 2 on the left. The corresponding force is determined by a piezo load cell that is integrated into the testing machine. Tests were conducted at room temperature in order to quantify the adiabatic heating in the fracture region of the sample. A thermal camera VarioCam with a maximum frame rate of 1000 was used to measure the temperature change during the test. For this purpose, the back side of the specimen is painted black as shown in Figure 2 in the middle. The maximum acceleration distance to reach the test speed is 150 mm, as the outer cage moves downwards at the start of the test and would otherwise press on the upper specimen grip. The thermal camera allows observing the temperature distribution in the complete measurement area at discrete time steps. The wavelength range for the thermocamera is 3–5 µm and emissivity is equal to 0.91. However, for the necessary resolution of the pictures of 640 × 480 pixels, the frame rate is limited to 1000 frames per second.

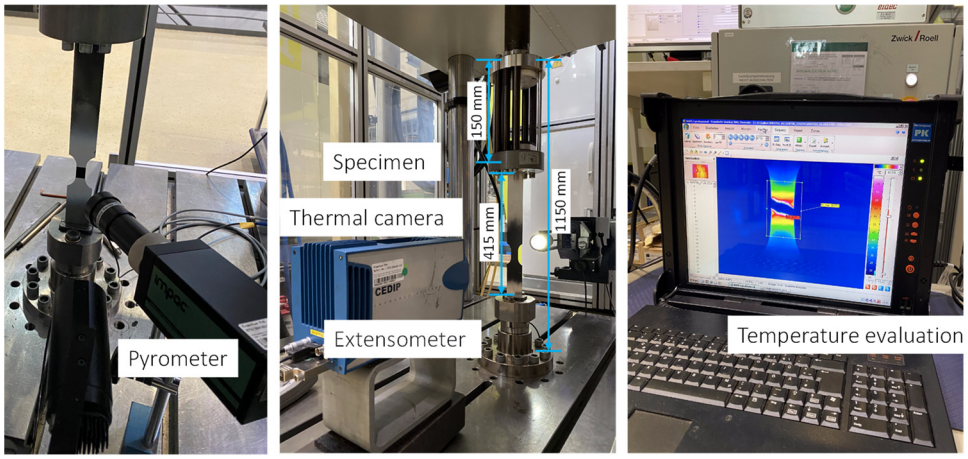

Figure 2. Experiment setup including high-speed thermal camera and pyrometer.

In preliminary tests, it was found that this frame rate is sufficient to observe the time-dependent development of the temperature distribution for test speeds in the magnitude of up to 1 m/s and corresponding strain rates of up to 50/s. For higher tests speeds, it is no longer possible to obtain a sufficient number of pictures during the test to draw reliable conclusions regarding the temperature development during the test and specifically to observe the temperature during failure of the specimen.

To overcome this restriction, a high-speed pyrometer IGA 740 from Lumasense, with a frequency of scanning of about 160 kHz, was used in addition to the thermal camera. It allows observing the time-dependent mean temperature in a small stationary area—a measurement point with a diameter of 1 mm. As the specimen is elongated during the tensile test, this measurement point moves over the sample so that the temperature data cannot be attributed to a specific point of the specimen, a fact which has to be considered when interpreting the measurement data and comparing it with numerical results.

In order to allow capturing the maximum temperature reached in the failure area of the specimen directly before fracture, further preliminary tests were performed in order to estimate the distance that the measurement point moves during the experiment and set its start position correspondingly. As shown in Figure 3, the measuring point was positioned in the axial middle of the specimen and close to the edge of the measurement area for the extensometer before the test (Figure 3a), so that the extension of the measuring length of the sample would shift exactly to the position of the expected fracture (Figure 3b) to measure the maximum temperature reached at that moment.

2.3. Finite Element Method

FE Analysis was performed using an explicit thermal and mechanical solver in the commercial LS DYNA software. The flow behavior of the material is modeled via the classical *MAT_024_PIECEWISE_LINEAR_PLASTICITY model [23] using different flow curves in order to consider strain-rate-dependency. The flow curves used for the simulation are shown in Figure 10. Damage and failure strain rate effects are considered via the GISSMO damage and failure model developed by Neukamm et al. [24]. This model combines the damage description, which is used to calculate the crash simulations, and an incremental formulation for the description of the material instability and localization. It is implemented in LS-DYNA by keyword *MAT_ADD_EROSION and enabled by setting IDAM = 1, the functions $\varepsilon_f(\eta)$, $\varepsilon_{krit}(\eta)$, and $\alpha(L_e)$ are defined as input parameters by keyword *DEFINE_CURVE and the parameters n and m are defined directly on the material card. The fracture parameters listed above were revealed by a combination of experimental studies of different sample geometries (in order to cover different triaxial states) and inverse modeling performed in LS-OPT. In more detail, these calculations are given in [15] but the basic fracture curves as well as the m and n parameters are presented in Figure 4.

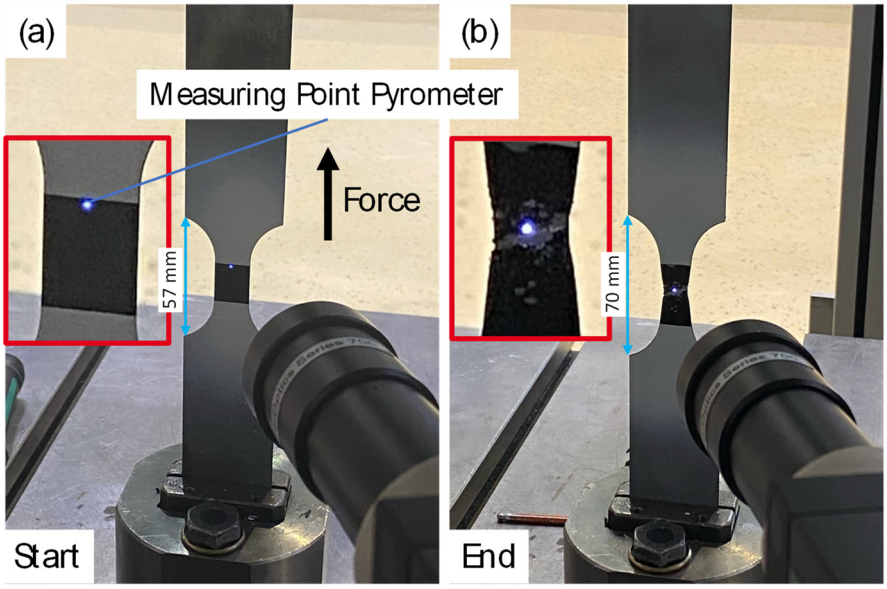

Figure 3. Experimental setup of temperature measurement with a pyrometer. (**a**) before the test and (**b**) after the test.

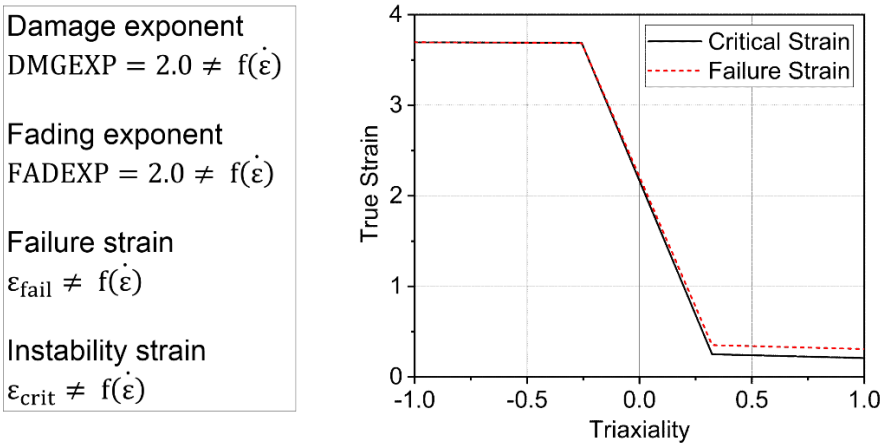

Figure 4. Damage parameters (failure strain).

The consideration of the nonlinearity of the strain path for the GISSMO model can be based on the fact that the damage is quantitatively accumulated stepwise for each change in the strain path [25]. The main focus of this study is the plastic component of the existing material model, namely, expanding it by adding yield curves for different strain rates. The input parameters used in the simulation were the data obtained experimentally, namely, the path of the traverse during the tests and the distance between the markers, which was measured with an extensometer. The experimentally determined input parameters for the simulation, in the form of the traverse displacement, are shown in Figure 5.

The simulations of the specimen tests were performed with fully integrated solid elements (ELFORM 2) with edge lengths of 0.5 × 0.5 × 0.1 mm and LS-DYNA R12.0.0. The geometry with dimensions of the sample used for simulation is shown in Figure 1. The choice of this finite element mesh size was justified by the fact that, even in preliminary work, this ratio allowed to obtain the best results for the fracture model in relation to the temperature distribution. In addition, the most exact comparability for the GISSMO fracture model is optimized for these element sizes in the previous work [15]. The used model included 30810 elements. One of the edges of the sample was fixed in place using the *BOUNDARY_SPC_SET* command and the other side was given an experimental

motion using *BOUNDARY_PRESCRIBED_MOTION_SET* obtained from the traverse of the high-speed testing machine as shown in Figure 6a.

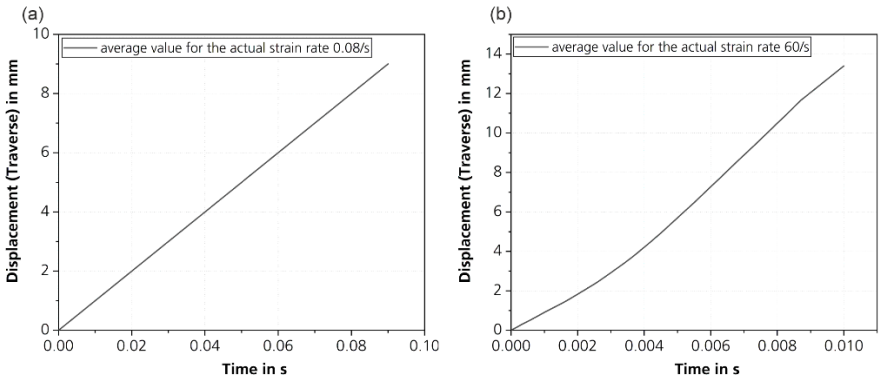

Figure 5. Displacement of the traverse during the tests for actual strain rates of (**a**) 0.08/s and (**b**) 60/s.

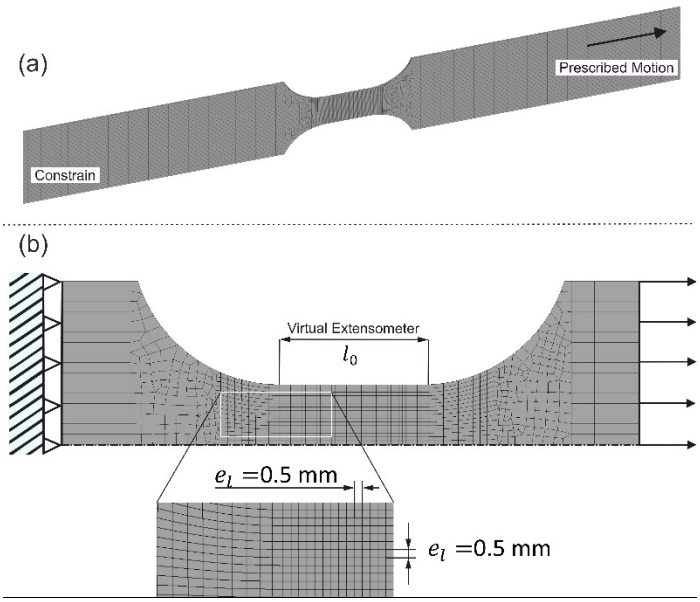

Figure 6. Finite element model of the—(**a**) specimen. (**b**) shows a detailed view of the virtual extensometer and the used element size.

In order to provide good comparability of the measured and the numerically determined data, the determination of the change in the parameter, l_0, in the sample was carried out similar to the measurement principle of the extensometer. As shown in Figure 6b, the elongation of the sample was evaluated by tracking the displacement of two points in the center of the sample, using the *HISTORY__NODE*.

The temperature distribution is calculated via the dissipated forming energy according to Equation (2) based on the temperature increase, $\Delta\vartheta$, the specific heat capacity, c_ϑ, the Taylor–Quinney factor, κ [26], and the forming work performed, ΔW_{dis}. The Taylor–Quinney factor is used to define the fraction of plastic stress power that is not converted into heat. For the thermomechanical calculations performed in LS-DYNA, $\kappa = 0.9$ was set.

$$\Delta\vartheta = \frac{\kappa \cdot \Delta W_{\mathrm{dis}}}{c_\vartheta \cdot \rho} \tag{2}$$

The output characteristics to be obtained from the simulation include temperature distribution, strain rate, elongation of the test sample, and the maximum force achieved during the test.

3. Results

3.1. Identification of Strain-Rate-Dependant Flow Curves

Frequently, Equation (1) is used to calculate a nominal strain rate based on the nominal traverse velocity set in a high-speed tensile test. This is a simple approach in order to provide a good approximation of the mean strain rate during a significant part of the test, specifically for the plastic deformation of the specimen until the onset of localization. However, it is obvious that the velocity of the traverse during the test is subject to the control of the machine and, consequently, the actual strain rate can vary during the test due to inaccuracies in this control. In order to determine the actual strain rate, the displacement of the traverse was recorded and the time derivative was calculated in order to obtain the traverse velocity, which was in turn referred to the measurement length according to Equation (1). Figure 6 presents the actual course of the strain rates as a function of the elongation for all test speeds considered in this study. It can be seen that the strain rate at the start of the test is significantly below the nominal value. Furthermore, there is a transient phenomenon at the start, which can probably be attributed to the measurement technique. As the test progresses, the strain rate in the specimen approaches the respective target value and remains at a relatively constant level. Finally, at the end of the test, the curve rises again and reaches values that are significantly higher than the nominal strain rate. This is probably due to the localization of the strain and the initiation of fracture. Based on this typical course or the curves, an average value of the strain rate for the entire test was identified and is indicated in Figure 7 as the actual value. The deviation of the nominal and the actual strain rate values varies from 10% to 20% in the range of strain rates considered here. It is important to consider this deviation when attributing the flow curves measured during the high-speed tensile test to a specific strain rate.

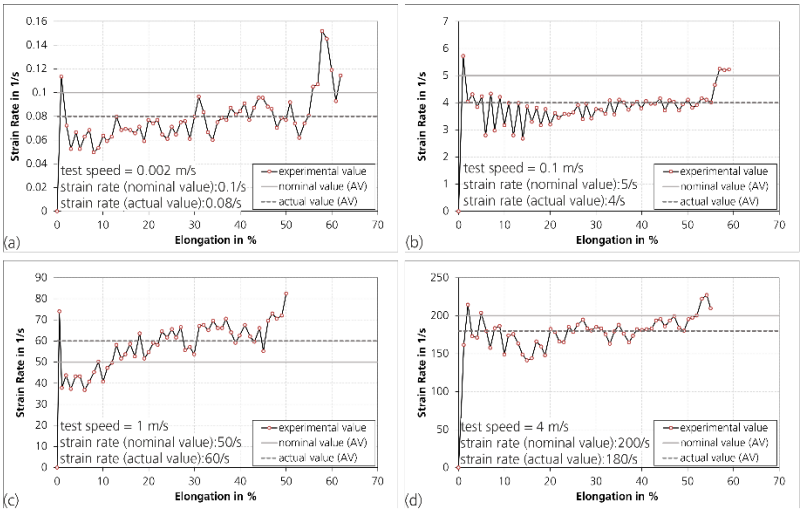

Figure 7. Nominal and actual values of the strain rate obtained during the tests for nominal strain rate 0.1/s (**a**), 5/s (**b**), 50/s (**c**), and 200/s (**d**).

Figure 8 exemplarily shows the yield curves obtained from the three experiments performed at an actual strain rate of 0.08/s (i.e., a nominal strain rate of 0.1/s) as well as the mean values from these measurements. Based on this, a flow curve approximation according to Swift/Hockett–Sherby was calculated (see Equation (3)) and extrapolated up to a degree of deformation of 1.0.

$$\sigma_F = (1 - K_1)[K_2(K_3 + \varphi)^{K_4}] + K_1[K_5 - (K_5 - K_6)e^{-K_7\varphi^{K_8}}] \quad (3)$$

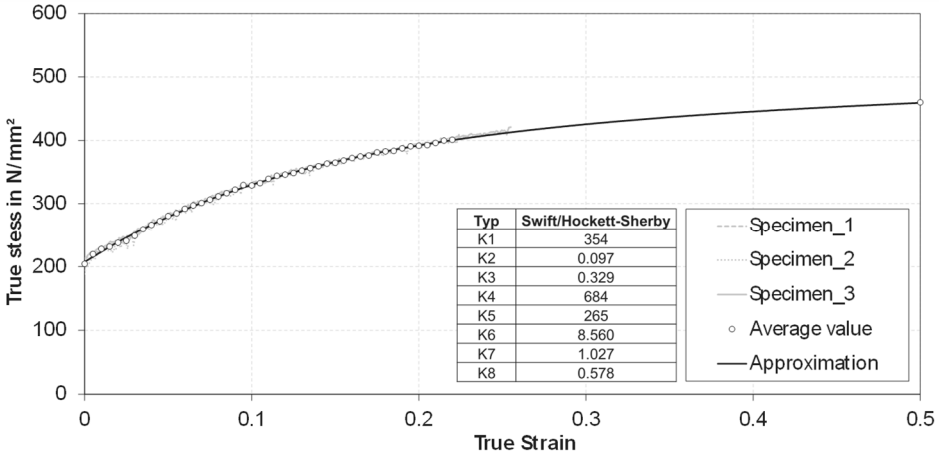

Figure 8. The yield curve of the material DC06 for an actual strain rate of 0.08/s.

In Equation (3), σ_F is the yield stress and φ is the degree of deformation. An Excel solver was used to adjust the function to the measured flow curve and to calculate the parameters K_1 to K_8. Figure 8 also provides the calculated parameters and the approximated yield curve at an actual strain rate of 0.08/s. There is a very good agreement between the calculated and measured values.

Here, the curve obtained for an actual strain rate of 0.08/s was taken as the basis for the approximation, which was subsequently approximated according to Equation (4), using conditional coefficients, C_1 and C_2, as well as experimental data for the strain rates studied. The logarithmic dependence on the strain rate and the values of these coefficients for the tested actual strain rates of 4, 60, and 180/s are shown in Figure 9.

$$\sigma = f(\varphi) = \sigma_f \cdot C_1 + \frac{\sigma_{f,0}}{C_2} \tag{4}$$

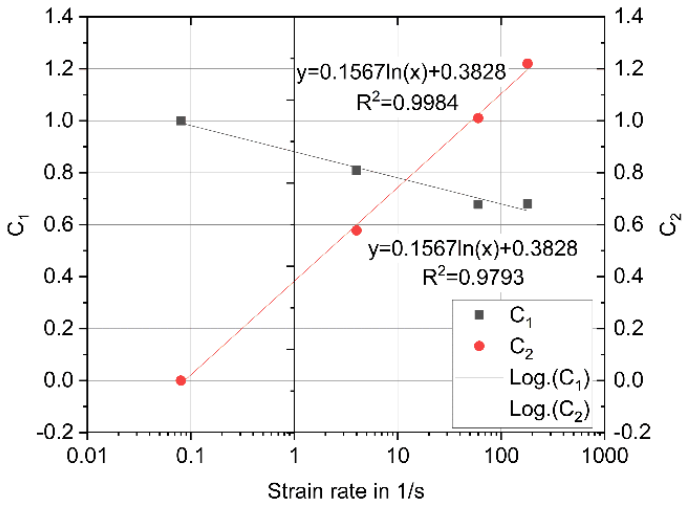

Strain rate	C_1	C_2
0.008	1	0
4	0.81	0.57
60	0.67	1
180	0.68	1.22

Figure 9. Logarithmic dependency of coefficients C_1 and C_2 on the strain rate.

The yield curves for the subsequent higher strain rates tested, together with the approximated curves, are shown in Figure 10. Obviously, the approximation method used shows good agreement with the experimental data; this is especially noticeable for actual strain rates of 0.08 and 4/s. From an actual strain rate of 60/s, the curve of real values has a wavier shape, which is even more noticeable for an actual strain rate of 180/s because of the high strain rate. However, the approximated values are still close to the experimental data.

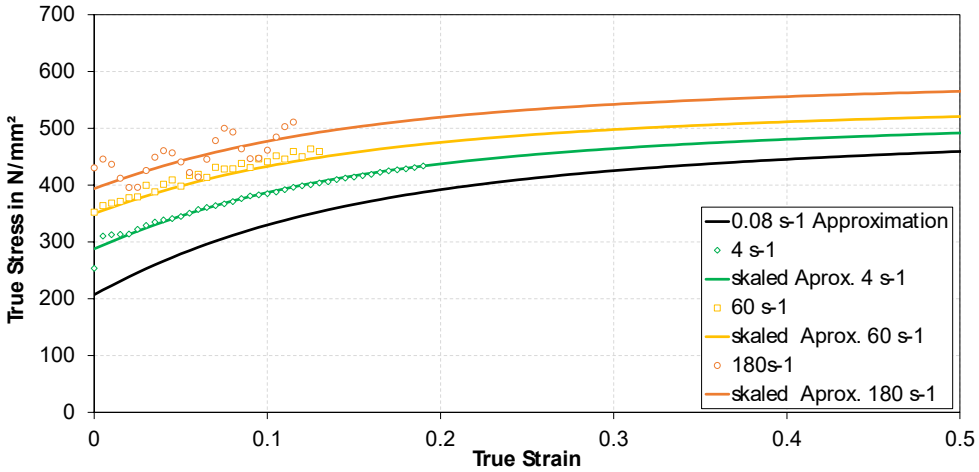

Figure 10. Approximated yield curves for actual strain rates of 0.08/s, 4/s, 60/s, and 180/s.

3.2. Numerical Simulation of the Tensile Test and Experimental Validation of Force and Temperature Values

As mentioned above, the determination of the mean strain rate via Equation (1) provides a good approximation of the strain rate as long as the specimen deformation is uniform. As soon as localization occurs, the strain rate is no longer distributed homogenously in the specimen. It rises quickly in the areas of localization and the local strain rate in the fracture zone is much higher than the analytically calculated nominal and actual values. This can be clearly seen in Figure 11. This figure compares the strain rate courses obtained from the simulation for individual elements near and slightly beyond the fracture zone of the sample for the four considered strain rates. At the beginning of the test, the strain rates are very similar for all elements in the specimen, but with further progress, the curves start to deviate from each other. The strain rate of element 1 that is located in the middle of the specimen rises dramatically, while the strain rates of elements 2 and 3 tend to remain on the same level for some more time and finally decrease. This clearly reflects the localizing of the strain and the strain rate in that region of the specimen, where damage and finally failure of the material can be observed.

Therefore, the range of strain-rate-dependent flow curves necessary for realistically modeling damage and failure significantly exceeds the nominal and actual strain rates defined for the test in Section 3.1. For this reason, auxiliary yield curves were additionally approximated using Equation (3). A logarithmic relationship for three different true strain values as a function of strain rate was used as a reference as shown in Figure 12. This allowed an extended material model with strain rate dependence to be used when simulating the LS DYNA uniaxial tensile test.

In order to verify the material model, numerically calculated and measured force-displacement curves for actual strain rates of 0.08/s and 60/s were compared (see Figure 13). Up to the maximum stress, the agreement is very good. However, as soon as necking starts, the stress state becomes multiaxial, and the softening is different. This results in a deviation of measured and numerically determined displacement and strain at failure in the range of 10%.

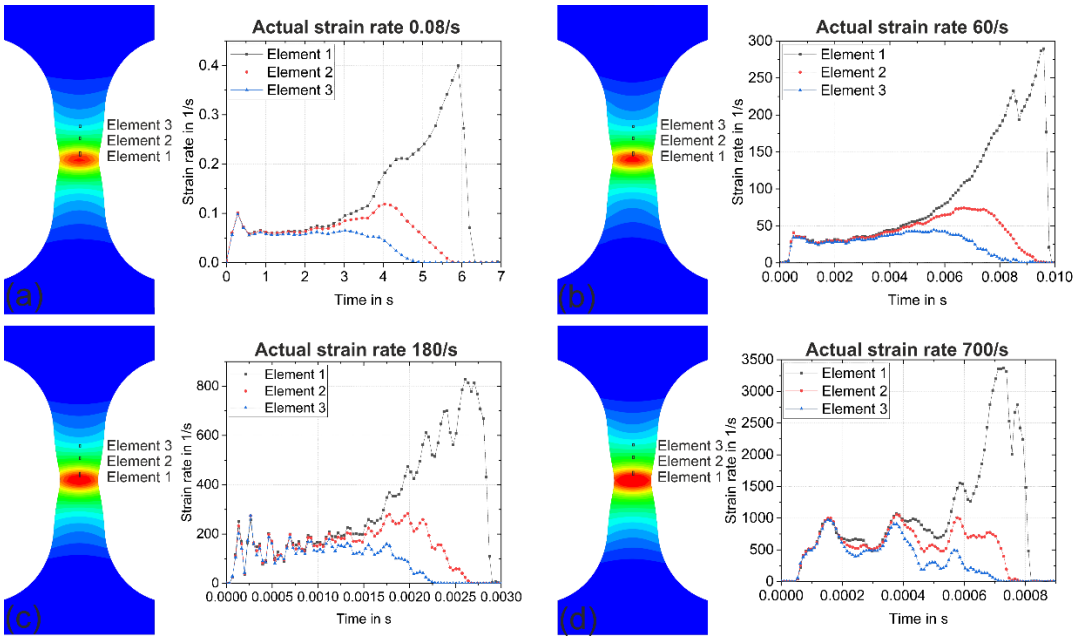

Figure 11. Comparison of strain rate values for individual elements obtained from process simulations for actual strain rates of 0.08/s (**a**), 60/s (**b**), 180/s (**c**), and 700/s (**d**).

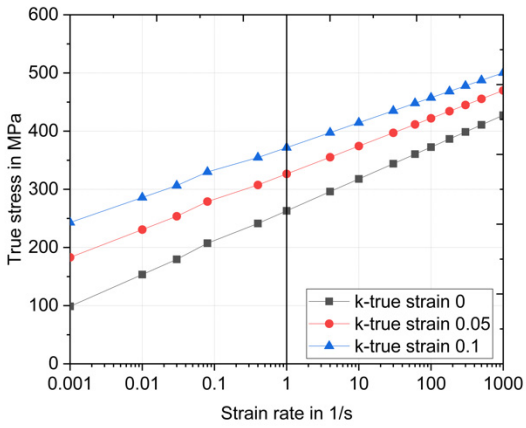

Figure 12. Logarithmic dependence of strain rate and yield strength for three different degrees of true strain.

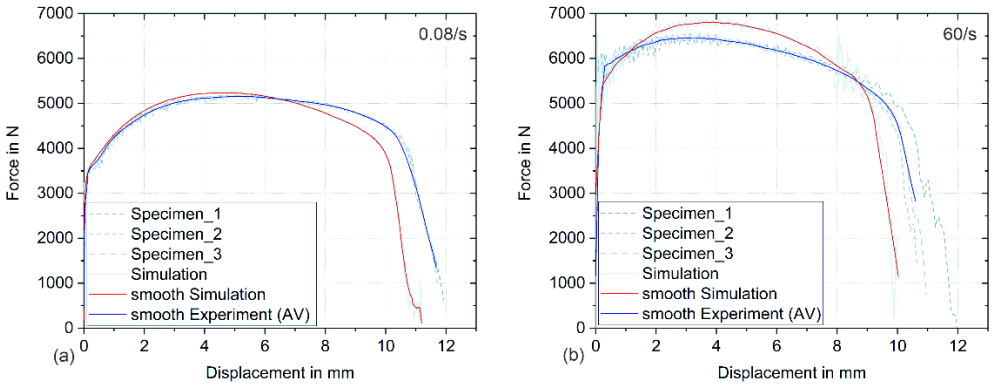

Figure 13. Comparison of experimental force-displacement curves with simulation results for actual strain rates of (**a**) 0.08/s and (**b**) 60/s.

For further validation, the temperature reached in the fracture region was recorded in simulation and experiment for actual strain rates from 0.08/s to 700/s. Considering an actual strain rate of 0.08/s as an example, Figure 14 compares the thermal camera data with simulation data for three significant stages of the test process: shortly before fracture, at the moment of fracture, and after complete fracture of the sample. The comparison shows good qualitative and quantitative agreement of simulation and experiment with a deviation of the maximum temperature of less than 7% until the onset of fracture. After fracture, however, the quantitative deviation of the maximum temperature rises significantly. The reason for this may be premature removal of the element in question, which does not have time to reach the required temperature, due to destruction, namely, reaching the value set in the parameters of the GISSMO.

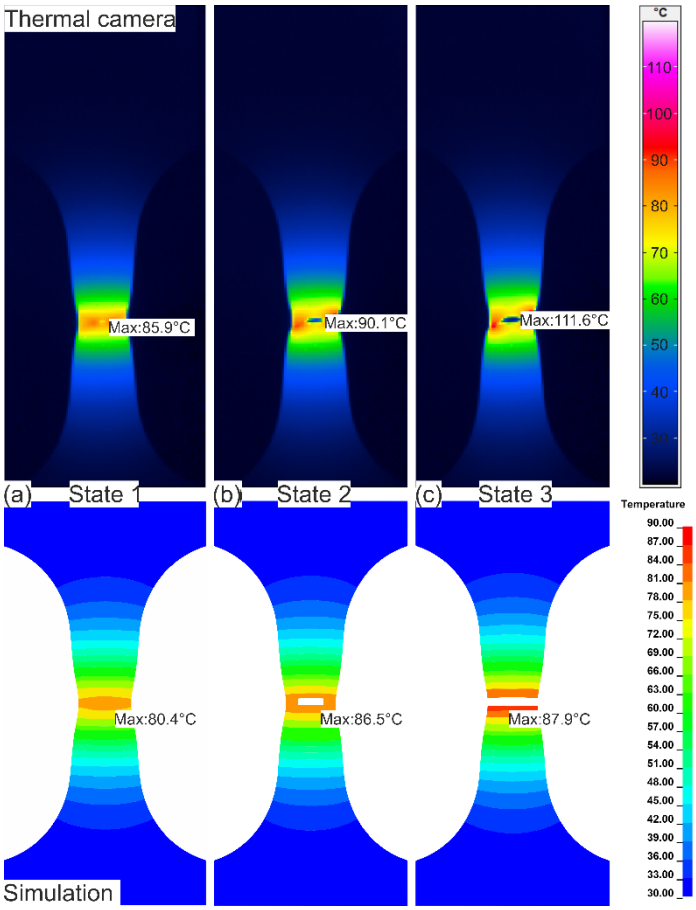

Figure 14. Comparison of the experimentally measured temperature value of the sample using the thermal camera with the simulation values for the strain rate of 0.1 for state 1: before failure (**a**), state 2: failure already initiated (**b**), and state 3: after failure (**c**).

Figure 15 summarizes and compares the measured and numerically calculated maximum temperature in the fracture region as a function of the strain rate. For each strain rate considered in this study, the experimental data comprises the mean value and the maximum deviation from this value determined on the basis of three tests performed with the same process parameters. The figure shows that, as expected, the temperature rises quickly with increasing strain rate. For the considered range of strain rates, there seems to be a nearly linear correlation between the temperature and the logarithmically plotted strain rate. In general, numerical and experimental results are in good agreement with each other. The largest discrepancy exists between the low strain rate and the measurement with the thermocamera. For the higher strain rates, measurements were made with the high-speed pyrometer, which seem to agree better with the simulation compared with the

thermal camera. Direct comparison of the results of the two measurement systems is only possible for a very limited temperature range because the pyrometer can only measure temperatures above 160 °C, while the camera is limited to capturing maximum temperature of the tests with low strain rates due to the limited frame rate (compare Section 2.2). However, in spite of this, it was possible to obtain good comparability for testing at a strain rate of 50/s between the thermal camera and the pyrometer, as shown in Figure 16.

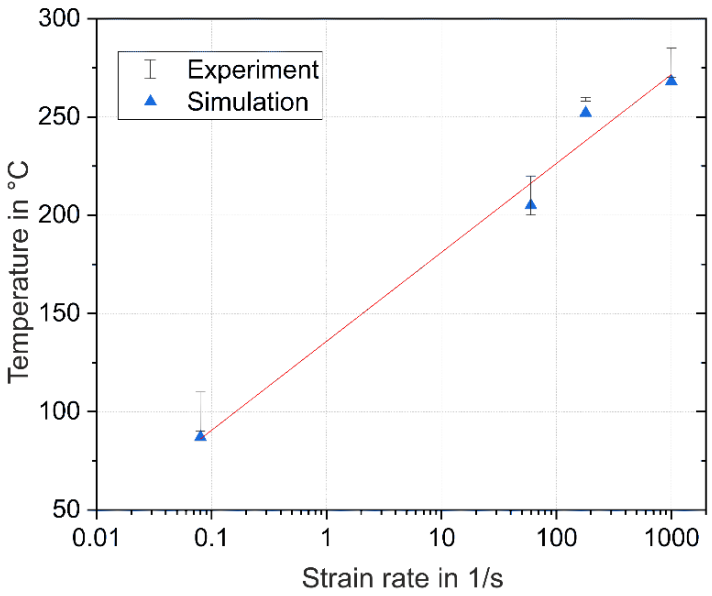

Figure 15. Comparison of experimentally measured temperature values and simulation results for actual strain rates of 0.08/s, 60/s, 180/s, and 700/s.

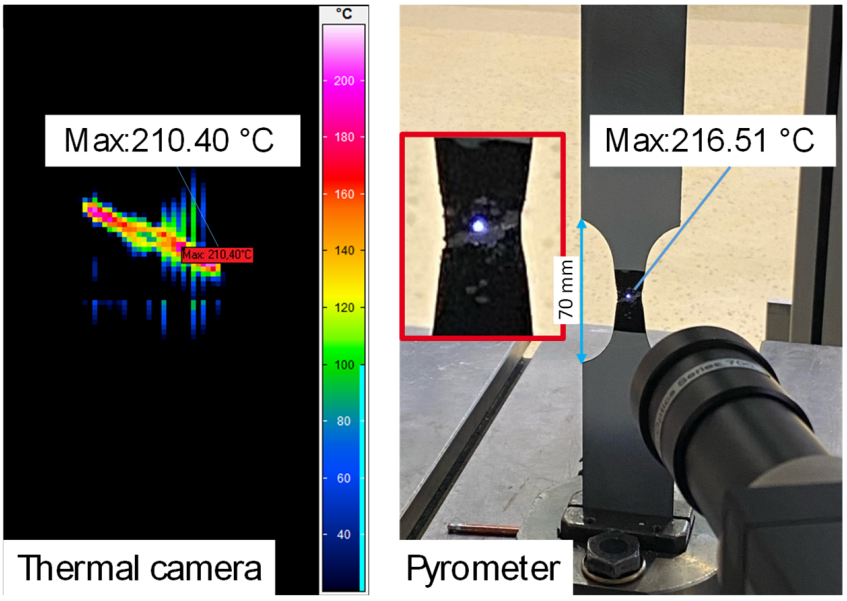

Figure 16. Comparison of temperature values obtained from the thermal camera and pyrometer for a nominal strain rate of 50/s.

4. Discussion

In this work, we investigated the effects of strain rate as well as temperature changes in the fracture region for the DC06 steel in order to obtain a deeper understanding of the correlations between strain rate hardening and thermal softening under high-speed loading. The study is based on high-speed tensile tests because the simple setup of these

tests allows precise observation of the force, the corresponding deformation, and the temperature development during the process. The experimental tests were complemented by numerical simulation of the testing procedure. For this purpose, a material model made as simple as possible but still with sufficient accuracy to predict the temperature development was sought.

By simulation in LS DYNA, as described in Section 2.3, the Taylor–Quinney factor was set to 0.9, which allowed a good comparability for simulation and experiment. However, in future works, it would be interesting to investigate this parameter as a function of strain rate, as was done in [21,27].

Creating a material model that is close to the real process begins with a properly performed test, which includes a sufficient number of samples tested in the required range of strain rates. As shown in Figure 6, the nominal strain rate calculated on the basis of the nominal test speed of the machine does not always correspond to the actual strain rate. Naturally, the absolute deviation increases with increasing strain rate, e.g., at a strain rate of 0.1, the actual strain rate was 0.08 (deviation 0.02), at higher strain rates such as 200/s, the actual strain rate was already only 180/s (deviation 20/s). The relative deviation, however, is in the range of 20% of the target value for most strain rates considered here. As a consequence of this inaccuracy, it is decisive to record the actual test speed and attribute the identified material behavior to the corresponding actual strain rate.

Furthermore, it is necessary to make a sophisticated choice of the range of strain rates that are considered in the material model. Here, it must be taken into account that localization effects are associated with strain rates that can exceed the nominal strain rate in the test by many times. Successfully selected yield curves for the corresponding strain rates can serve as the basis for increasing the range of the material model through simple approximations (Figure 11).

5. Conclusions

Using this extended material model, good comparability with experimental results can be achieved. This can be seen particularly well in Figure 12. Especially in the area of elastic deformation (characterized by Young's modulus) and plastic deformation up to the uniform elongation (characterized by the maximum force value), good agreement between experiment and simulation is achieved and even with regard to the elongation at fracture, the 10% deviation of the numerical and experimental results is still acceptable. Moreover, the temperature development was predicted by the numerical simulation with good accuracy for all strain rates considered in this study (see Figures 13 and 14).

Thus, our study provides the following important results and conclusions:

- Taking into account the actual strain rate for each of the tests performed is necessary since this value is often not the same as the set value for the machine.
- The plastic material model must take into account a range of strain rates exceeding the nominal strain rate of the test by several times in order to reproduce localization effects with sufficient accuracy.
- The sophisticated choice of the measuring point allows recording the maximum temperature in the fracture region with a high-speed pyrometer for strain rates of up to several hundred per second.
- The results of the experiment and simulation are well comparable using the provided material model.

Author Contributions: Conceptualization, E.G., S.W., F.R. and V.P.; methodology, E.G. and V.P.; software, E.G., F.R. and M.T.; validation, E.G., F.R. and V.P.; investigation, E.G.; resources, V.P. and V.K.; writing—original draft preparation, E.G.; writing—review and editing, E.G., S.W., F.R. and V.P.; visualization, E.G.; supervision, V.P., V.K. and A.B.; project administration, E.G. and V.P.; funding acquisition, V.P. All authors have read and agreed to the published version of the manuscript.

Funding: This research was funded by the Deutsche Forschungsgemeinschaft (DFG, German Research Foundation), grant numbers PS 68/2-3 and BR 3500/19-3.

Data Availability Statement: Not applicable.

Conflicts of Interest: The authors declare no conflict of interest. The funders had no role in the design of the study; in the collection, analyses, or interpretation of data; in the writing of the manuscript, or in the decision to publish the results.

References

1. Avrillaud, G.; Mazars, G.; Cantergiani, E.; Beguet, F.; Cuq-Lelandais, J.-P.; Deroy, J. Examples of How Increased Formability through High Strain Rates Can Be Used in Electro-Hydraulic Forming and Electromagnetic Forming Industrial Applications. *JMMP* **2021**, *5*, 96. [CrossRef]
2. Psyk, V.; Scheffler, C.; Stalmann, A.; Goede, M. Shaping of Sharp-Edged Design Elements by Electromagnetic Forming. In *Forming the Future*; Springer: Berlin/Heidelberg, Germany, 2021; pp. 1315–1327.
3. Rohatgi, A.; Stephens, E.V.; Soulami, A.; Davies, R.W.; Smith, M.T. *High-Strain-Rate Forming of Aluminum and Steel Sheets for Automotive Applications*; Pacific Northwest National Lab.(PNNL): Richland, WA, USA, 2010.
4. Li, Z.; Voisin, T.; McKeown, J.T.; Ye, J.; Braun, T.; Kamath, C.; King, W.E.; Wang, Y.M. Tensile properties, strain rate sensitivity, and activation volume of additively manufactured 316L stainless steels. *Int. J. Plast.* **2019**, *120*, 395–410. [CrossRef]
5. Boyce, B.L.; Dilmore, M.F. The dynamic tensile behavior of tough, ultrahigh-strength steels at strain-rates from 0.0002 s^{-1} to 200 s^{-1}. *Int. J. Impact Eng.* **2009**, *36*, 263–271. [CrossRef]
6. Liang, Z.Y.; Wang, X.; Huang, W.; Huang, M.X. Strain rate sensitivity and evolution of dislocations and twins in a twinning-induced plasticity steel. *Acta Mater.* **2015**, *88*, 170–179. [CrossRef]
7. Pouya, M.; Winter, S.; Fritsch, S.; Wagner, M.F.-X. A numerical and experimental study of temperature effects on deformation behavior of carbon steels at high strain rates. *IOP Conf. Ser. Mater. Sci. Eng.* **2017**, *181*, 12022. [CrossRef]
8. Johnson, G.R.; Cook, W.H. Fracture characteristics of three metals subjected to various strains, strain rates, temperatures and pressures. *Eng. Fract. Mech.* **1985**, *21*, 31–48. [CrossRef]
9. Gurson, A.L. Continuum theory of ductile rupture by void nucleation and growth: Part I—Yield criteria and flow rules for porous ductile media. *J. Eng. Mater. Technol.* **1977**, *99*, 2–15. [CrossRef]
10. Tvergaard, V.; Needleman, A. Analysis of the cup-cone fracture in a round tensile bar. *Acta Metall.* **1984**, *32*, 157–169. [CrossRef]
11. Praveen Kumar, A.; Shrivaathsav, S. Influence of forming parameters on the crash performance of capped cylindrical tubes using LS-DYNA follow-on simulations. *Int. J. Interact. Des. Manuf. (IJIDeM)* **2019**, *13*, 1215–1232. [CrossRef]
12. Feucht, M.; Neukamm, F.; Haufe, A.A. A phenomenological damage model to predict material failure in crashworthiness applications. In *A Phenomenological Damage Model to Predict Material Failure in Crashworthiness Applications*; Recent developments and innovative applications in computational mechanics, Ed.; Springer: Berlin/Heidelberg, Germany, 2011; pp. 143–153.
13. Andrade, F.X.C.; Feucht, M.; Haufe, A.; Neukamm, F. An incremental stress state dependent damage model for ductile failure prediction. *Int. J. Fract.* **2016**, *200*, 127–150. [CrossRef]
14. Winter, S.; Nestler, M.; Galiev, E.; Hartmann, F.; Psyk, V.; Kräusel, V.; Dix, M. Adiabatic Blanking: Influence of Clearance, Impact Energy, and Velocity on the Blanked Surface. *JMMP* **2021**, *5*, 35. [CrossRef]
15. Psyk, V.; Scheffler, C.; Tulke, M.; Winter, S.; Guilleaume, C.; Brosius, A. Determination of Material and Failure Characteristics for High-Speed Forming via High-Speed Testing and Inverse Numerical Simulation. *JMMP* **2020**, *4*, 31. [CrossRef]
16. Boz, Z.; Erdogdu, F.; Tutar, M. Effects of mesh refinement, time step size and numerical scheme on the computational modeling of temperature evolution during natural-convection heating. *J. Food Eng.* **2014**, *123*, 8–16. [CrossRef]
17. Li, Y.N.; Karr, D.G.; Wang, G. Mesh size effects in simulating ductile fracture of metals. In Proceedings of the 10th International Symposium on Practical Design on Ships and Other Floating Structures, Houston, TX, USA, 1–5 October 2007; pp. 247–254.
18. Lorenz, D.; Haufe, A. Recent advances and new developments in hot forming simulation with LS-DYNA. In Proceedings of the Numisheet2008 Proceedings, Interlaken, Switzerland, 1–5 September 2008.
19. Gao, Y.; Wagoner, R.H. A simplified model of heat generation during the uniaxial tensile test. *Metall. Trans. A* **1991**, *18*, 1001–1009. [CrossRef]
20. Raghavan, K.S.; Wagoner, R.H. Combined influence of geometric defects and thermal gradients on tensile ductility. *Metall. Trans. A* **1987**, *18*, 2143–2150. [CrossRef]
21. Knysh, P.; Korkolis, Y.P. Determination of the fraction of plastic work converted into heat in metals. *Mech. Mater.* **2015**, *86*, 71–80. [CrossRef]
22. Majidi, O.; Barlat, F.; Korkolis, Y.P.; Fu, J.; Lee, M.-G. Thermal effects on the enhanced ductility in non-monotonic uniaxial tension of DP780 steel sheet. *Met. Mater. Int.* **2016**, *22*, 968–973. [CrossRef]
23. Andrade, F.; Feucht, M. A Comparison of Damage and Failure Models for the Failure Prediction of Dual-Phase Steels. In Proceedings of the 11th European LS-DYNA Conference, Salzburg, Austria, 9–11 May 2017.
24. Neukamm, F.; Feucht, M.; Haufe, A.; Roll, K. On closing the constitutive gap between forming and crash simulation. In Proceedings of the 10th International LS-DYNA Users Conference, Dearborn, MI, USA, 8 May 2008; pp. 12–21.
25. Volk, W.; Suh, J. Prediction of formability for non-linear deformation history using generalized forming limit concept (GFLC). In *AIP Conference Proceedings*; American Institute of Physics: College Park, MD, USA, 2013; pp. 556–561, ISBN 0735411956.

26. Taylor, G.I.; Quinney, H. The latent energy remaining in a metal after cold working. *Proc. R. Soc. London. Ser. A Contain. Pap. A Math. Phys. Character* **1934**, *143*, 307–326.
27. Żaba, K.; Trzepieciński, T.; Puchlerska, S.; Noga, P.; Balcerzak, M. Coupled Thermomechanical Response Measurement of Deformation of Nickel-Based Superalloys Using Full-Field Digital Image Correlation and Infrared Thermography. *Materials* **2021**, *14*, 2163. [CrossRef]